Ecotoxicology and Environmental Safety 159 (2018) 332–341

Contents lists available at ScienceDirect

Ecotoxicology and Environmental Safety

journal homepage: www.elsevier.com/locate/ecoenv

Synthesis of mesoporous triple-metal nanosorbent from layered double hydroxide as an efficient new sorbent for removal of dye from water and wastewater

Miloš Kostić[a,*], Miljana Radović[a], Nena Velinov[a], Slobodan Najdanović[a], Danijela Bojić[a], Andrew Hurt[b], Aleksandar Bojić[a]

[a] Department of Chemistry, Faculty of Science and Mathematics, University of Niš, Višegradska 33, 18 000 Niš, Serbia
[b] Faculty of Engineering and Science, University of Greenwich, Chatham Maritime, Kent ME4 4TB, UK

ARTICLE INFO

Keywords:
Layered double hydroxide
Mesoporous triple-metal nanosorbent
Reactive Blue 19
Kinetics
Isotherms
Wastewater

ABSTRACT

In this study, co-precipitation synthesis of the mesoporous triple-metal nanosorbent from Fe, Cu, Ni layered double hydroxide (FeCuNi-LDH), on the basis of the data obtained from the TG analysis was carried out. The FTIR spectroscopy and XRD results confirm the formation of CuO, NiO and Fe_2O_3 nanoparticles, while the EDX analysis does not show significant variations on the surface in elemental composition. BET analysis shows that FeCuNi-280 (FeCuNi-LDH calcinated at 280 °C) with mesoporous structure, has larger surface area compared to FeCuNi-LDH and FeCuNi-550 (FeCuNi-LDH calcinated at 550 °C). The value of pH_{PZC} of FeCuNi-280 is found to be 8.66. Obtained FeCuNi-280 material showed the ability for efficient removal of dye Reactive Blue 19 (RB19) from water, with a very high sorption capacity of 480.79 mg/g at optimal conditions: the sorbent dose of 0.6 g/dm^3, stirring speed of 280 rpm and pH 2. The kinetics results of the sorption process were well fitted by pseudo-second order and Chrastil model, and the sorption isotherm was well described by Sips, Langmuir and Brouers–Sotolongo model. FeCuNi-280 was easily regenerated with aqueous solution of NaOH, and reutilization was successfully done in five sorption cycles. The present study show that easy-to-prepare, relatively inexpensive nanosorbent FeCuNi-280 is among the best sorbents for the removal of RB19 dye from water solution and wastewater from textile industry in wide range of pH.

1. Introduction

Environmental contamination by organic pollutants, as reactive textile dyes, has severe and chronic effects on living organisms, and it is one of a major problems that society faces today (Salleh et al., 2011). About 10,000 different types of dyes are used in many industries such as textile, paint, ink, plastics and cosmetics. Some 10–20% of these dyes are discharged into the wastewater stream after use in dyeing and finishing (Zubieta et al., 2008). Dyes are chemically and photolytically stable and originally produced to be resistant to the weather, light, water, and detergents. Reactive dyes are highly soluble in water. As effluents they contain environmentally problematic compounds and influence reduced water transparency and sunlight penetration, thereby altering photosynthetic activity and gas solubility (Bergamini et al., 2009). Reactive Blue 19 (RB19) or disodium salt of 1-amino-2-sulfo-4-(3-sulfoxy-ethyl-sulfophenyl-1-ylamino)-5,10-anthraquinone is one of the very stable and resistant anionic dye: it may be mutagenic and toxic because of the presence of electrophilic vinyl sulfone groups (Moghaddam et al., 2010).

Numerous techniques such as biological treatments, membrane filtration, electrochemical technology, advance oxidation processes and sorption process are used for the removal of dyes from water. Among them, sorption has been frequently used because of its high efficiency, economic feasibility, and operational simplicity (Xiao et al., 2016; Saeed et al., 2005). Many sorbents have been tested in attempts to reduce dye concentrations from aqueous solutions, such as carbon nanotubes (Karimifard and Moghaddam, 2016), paper sludge activated with potassium fluoride (Auta and Hameed, 2014), modified bentonite (Özcan et al., 2007; Gök et al., 2010), hydrolytic and aerobic microorganisms (Wang et al., 2009), g-MnO_2/MWCNT nanocomposite (Fathy et al., 2013), magnetic Fe_3O_4 nanoparticles modified by pyrrole (Shanehsaz et al., 2015), silica (Banaei et al., 2017a, 2017b), chitosan (Nga et al., 2016), MgO nanoparticles (Moussavi and Mahmoudi, 2009; Nga et al., 2013) and biosorbents (Çiçek et al., 2007; Shirzad-Siboni et al., 2014; Zhang et al., 2003).

Layered double hydroxides (LDH), known as anionic clays or hydrotalcite clays, have been investigated because of their tunable charge

* Corresponding author.
E-mail addresses: milos.kostic@pmf.edu.rs, mk484475@gmail.com (M. Kostić).

https://doi.org/10.1016/j.ecoenv.2018.05.015
Received 6 February 2018; Received in revised form 2 May 2018; Accepted 5 May 2018

density and wide application prospects. LDH have been widely used as catalysts, drug delivery materials, sorption and flame retardants. LDH provide the possibility of a high sorption capacity because of the large surface area, easy manipulation of sorption sites, morphology/pore structure and interlayer ion exchange (Cai et al., 2018). LDH as sorbents are characterized by high sorption capacity, low cost and non-toxicity. After calcination, LDH may be converted into mixed metal oxides. Likewise, the calcined product can be reconstructed into original layered structure in the aquatic environment (Lei et al., 2017; Lv et al., 2006). LDH materials can be represented by the general formula: $[M^{2+}_{1-x}M^{3+}_{x}(OH)_2]^{x+} \times [A^{n-}_{x/n} \times mH_2O]$.

In this study, a novel process of synthesis of a mesoporous triple-metal nanosorbent, has been developed. The structural characterizations of LDH (FeCuNi-LDH) and the nano-triple-metal nanosorbents have been performed through different techniques such as: Brunauer-Emmett-Teller (BET) method, x-rays diffraction (XRD), thermogravimetric analysis (TGA) for the thermal analysis, Fourier transform infrared spectroscopy (FTIR) to confirm the formation of nanosorbents, scanning electron microscopy (SEM) and energy-dispersive X-ray spectroscopy (EDS) to explore the surface morphology, size of the particles and elemental composition. The effect of different variables, including pH, temperature, sorbent dose, contact time and initial dye concentration was evaluated. The experimental results of RB19 sorption on nanosorbent FeCuNi-280 were analyzed using pseudo-first, pseudo-second-order, intra-particle diffusion and Chrastil's kinetic models and Langmuir, Freundlich, Sips and Brouers–Sotolongo isotherm models. The thermodynamics of the sorption was also evaluated. Regeneration and reusability of sorbent was studied. In order to confirm the efficiency of triple-metal nanosorbent FeCuNi-280 in real conditions, removal of RB19 from wastewater was carried out.

2. Materials and methods

2.1. Reagents

All chemicals were of reagent grade and used without further refinement. HNO_3, NaOH, NaCl, Na_2CO_3, $FeCl_3{\cdot}H_2O$, $FeCl_2{\cdot}4H_2O$, $NiCl_2{\cdot}6H_2O$, $CuCl_2{\cdot}2H_2O$, RB19, acetic acid and sodium salt of dodecylbenzene sulfonic acid were purchased from Merck (Darmstadt, Germany). Gleiton P was purchased from Polycoating GmbH (Brühl, Germany). All solutions were prepared with deionized water (18 MΩ).

2.2. Preparation of the nanosorbent

Nanosorbent was prepared by the novel hydrothermal process, using 6.76 g $FeCl_3{\cdot}6H_2O$, 4.97 g $FeCl_2{\cdot}4H_2O$, 4.26 g $CuCl_2{\cdot}2H_2O$ and 5.92 g $NiCl_2{\cdot}4H_2O$, dissolved in 50 ml of 0.1 M HCl solution, respectively. The solution was heated to 80 °C with a reflux condenser and mixed by agitating and ultrasonication (the power of ultrasound was 100 W/dm^3 and agitation speed 400 rpm), in period of 1 h. Then, 2 M NaOH solution was added dropwise, with the monitoring of the pH. The co-precipitation reaction was carried out at 80 °C with vigorous stirring and agitating with ultrasonication with refluxing. A brown colored precipitate was obtained at pH of about 10. After that, the suspension was continuously stirred and agitated with ultrasonication for 1 h. Following this, the mixture was allowed to settle for 2 h without stirring, ultrasonication and heating. The precipitate was washed several times with hot deionized water over a Büchner funnel. Finally, the prepared precipitate was dried at 90 °C for 24 h and abbreviated as FeCuNi-LDH. In the second step, the obtained FeCuNi-LDH was calcined in a furnace by being heated from room temperature to 280 °C and 550 °C with the gradient of 7 °C/min for 1 h. After calcination, the layered hydroxide structure was destroyed and changed into the triple-metal nanosorbent. Finally, the obtained solid aggregates of the triple-metal nanosorbent were crushed into powder and stored in an airtight plastic container for further use. The prepared triple-metal nanosorbents were abbreviated as FeCuNi-280 (calcinated at 280 °C) and FeCuNi-550 (calcinated at 550 °C).

2.3. Analysis and characterizations

RB19 concentration in the samples was determined using the UV–vis technique by the spectrophotometer Shimadzu UV–vis 1650 PC (Shimadzu, Japan), after filtration through a 0.45 μm membrane filter (Agilent Technologies, Germany). The infrared spectrum of nanosorbent FeCuNi was obtained by using a Fourier transform infrared spectrometer (Bomem Hartmann & Braun MB-100 spectrometer). The morphology of the nanosorbent surface was analyzed by SEM (Hitachi SU8030). EDS analysis (Thermo Scientific NORAN System 7, USA) provides elemental information via the analysis of X-ray emissions from the sorbent surface. Elemental composition was analyzed by the Perkin Elmer series II CHNS/O System Analyzer 2400. The specific surface area was measured by a nitrogen adsorption using the Micromeritics Gemini 5 Surface Area Analyzer, USA. Data were collected with a Bruker D8 Advance X-ray Diffractometer (Bruker, Germany) in theta-theta geometry in reflection mode with Cu Kα. TG analysis was performed using TGA Q5000 (TA Instruments, USA).

2.4. Batch sorption experiments

A stock solution of RB19 was prepared by dissolving an accurate quantity of dye in deionized water. The working standard solutions were prepared just before use by the appropriate dilution of the stock solutions. The sorption study was carried out using various RB19 concentration (20–700 mg/dm^3) at pH 2 and the temperature of 20 °C. The effect of pH on the RB19 sorption was studied in the pH range of 2.0–10.0. The pH of each solution was adjusted to the required value with 0.1/0.01 mol/dm^3 $NaOH/HNO_3$ solutions using a pH-meter (H260G, HACH, USA). The effects of FeCuNi-280 concentration on the removal of RB19 were studied by varying the dose of FeCuNi-280 from 0.125 to 1.0 g/dm^3 at 200 mg/dm^3 of the RB19 concentration, at pH 2 and the temperature of 20 °C. The temperature was held at 20.0 °C (± 0.2 °C) by thermostated bath Julabo F12-ED (Refrigerated/Heating Circulator, Germany). All experiments were conducted in triplicate.

The sorption capacity q_t (mg/g) and the removal efficiency (*RE* %) was determined by using the Eqs. 1 and 2:

$$q_t = \frac{(c_0 - c_t) \times V}{m} \quad (1)$$

$$RE\ \% = \frac{c_0 - c_t}{c_0} \times 100 \quad (2)$$

where c_0 and c_t are the initial and final concentrations of the dye in solution (mg/dm^3), V is the solution volume (dm^3) and m is the mass of the sorbent (g).

2.5. Desorption of RB19 and reused of triple-metal nanosorbent

In order to investigate the reusability performance of the triple-metal nanosorbent, five successive sorption–desorption (regeneration) cycles were performed. In adsorption test, 0.15 g of FeCuNi-280 was loaded with 250 cm^3 of RB19 solution with concentration of 200 mg/dm^3 and stirred for 180 min. After that, FeCuNi-280 was separated by centrifugation at 4000 rpm for 5 min and concentration of RB19 was determined in filtrate. To regenerate the adsorbent, the used FeCuNi-280 was contacted with 250 cm^3 of desorption solutions (0.1 M NaOH and 1 M NaCl), with stirring for 1 h. The sorption–desorption process was repeated for five times. The desorption efficiency (*DE* %) was calculated as follows:

$$DE\ \% = \frac{m_{\text{desorbed RB19}}\ [\text{mg}]}{m_{\text{previously sorbed RB19}}\ [\text{mg}]} \times 100 \quad (3)$$

2.6. Data analyses

In order to investigate the sorption mechanism of RB19 on triple-metal nanosorbent FeCuNi-280, confirm the efficiency of the sorption process and predict the rate, a kinetics investigation was conducted. The kinetics results were examined using two reaction-based kinetics models: pseudo-first-order (Eq. (4)) (Lagergren, 1898) and pseudo-second-order (Eq. (5)) (Ho and McKay, 1998) in their non-linearized forms, and a diffusion-based model: linearized intra-particle diffusion model (Eq. (6)) (Weber and Morris, 1963) and non-linearized form Chrastil's model (Eq. (7)) (Chrastil, 1990):

$$q_t = q_{e,cal}(1 - e^{-k_1 t}) \tag{4}$$

$$q_t = \frac{k_2 q_{e,cal}^2 t}{1 + k_2 q_{e,cal} t} \tag{5}$$

$$q_t = K_{id} t^{\frac{1}{2}} + C \tag{6}$$

$$q_t = q_{e,cal}\left(1 - e^{-k_c A_0 t}\right)^n \tag{7}$$

where q_t (mg/g) is sorption capacity in time (t), $q_{e,cal}$ (mg/g) is equilibrium sorption capacity of the sorbent, and k_1 (1/min) is the pseudo-first order reaction rate equilibrium constant, k_2 (g/mg min) is the rate constant of second order sorption, K_{id} (mg/g $min^{1/2}$) is the internal diffusion coefficient, C is the intercept and the foregoing parameters can be determined from a plot of q_t versus $t^{1/2}$ (the values of intercept give us an idea about the thickness of the boundary layer), k_c is a rate constant (dm^3/g min), which depends on diffusion coefficients and the sorption capacity of the sorbent, A_0 is the dose of the sorbent (g/dm^3) and n is the heterogeneous structural diffusion resistance constant, which range from 0 to 1. When diffusion resistance is small, n tends to 1 and the reaction is of first order. If the system is strongly limited by diffusion resistance, n is small. In addition, when $n > 1$, a consecutive reaction order may be expected (Witek-Krowiak, 2012).

Isotherm models provide fundamental physicochemical data to assess the sorption capacity and distribution of dye molecules between the liquid and solid phases. The collected sorption data were examined, employing several isotherm models, such as: Langmuir (Langmuir, 1918), Freundlich (Freundlich, 1906), Sips (McKay et al., 2014) and Brouers–Sotolongo (Brouers et al., 2005). The non-linear forms of the Langmuir (Eq. (8)), Freundlich (Eq. (9)), Sips (Eq. (10)) and Brouers–Sotolongo (Eq. (11)) models are represented below:

$$q_e = \frac{q_m K_L c_e}{1 + K_L c_e} \tag{8}$$

$$q_e = K_F c_e^{\frac{1}{n}} \tag{9}$$

$$q_e = \frac{q_m (b_S c_e)^n}{1 + (b_S c_e)^n} \tag{10}$$

$$q_e = q_m (1 - e^{(-K_W C_e^{\alpha})}) \tag{11}$$

where q_e is equilibrium sorption capacity of the sorbent (mg/g); c_e is the concentration (mg/dm^3) of RB19 at equilibrium time in solution; q_m is the maximum sorption capacity of the sorbent (mg/g); K_L is Langmuir constant related to the energy of sorption (dm^3/mg), K_F is the Freundlich equilibrium constant (mg/g) (dm^3/mg)$^{1/n}$ and n is the exponent; b_S (dm^3/mg) in Sips model is the affinity constant for sorption; K_W is Brouers–Sotolongo isotherm constant (dm^3/mg) and α is the Brouers–Sotolongo model exponent.

R_L is the separation factor or equilibrium parameter determined from the Langmuir isotherm for predicting whether a sorption system is favorable or unfavorable, can be estimated with Eq. (12):

$$R_L = \frac{1}{1 + K_L c_i} \tag{12}$$

The best fitting model was selected based on the determination coefficient values (r^2) determined after non-linear and linear regression analysis in the software OriginPro 2016 (OriginLab Corporation, USA) and the relative deviation of calculated q_e values from experimental q_e values was calculated by following equation:

$$\text{Relative deviation } \% = \frac{|q_{e,exp} - q_{e\text{ or }m,cal}|}{q_{e,exp}} \cdot 100 \tag{13}$$

where $q_{e,exp}$ is experimental sorption capacity in equilibrium (mg/g), $q_{e\text{ or }m,cal}$ (mg/g) is sorption capacity in equilibrium and calculated from the corresponding kinetic and isotherm model.

The relationship between kinetic parameters and sorption temperature (T) can be explained using Arrhenius's (Eq. (14)) (Mahmoud et al., 2012):

$$\log k_2 = -\frac{E_a}{2.303RT} + \text{constant} \tag{14}$$

where k_2 is the second-order rate constant, Ea is the activation energy, T is temperature (K) and R is universal gas constant (8.314 J/mol K).

The enthalpy change can be calculated using the Eq. (15) (Kumar et al., 2012):

$$E_a = \Delta H° + RT \tag{15}$$

3. Results and discussion

3.1. Characterization of materials

The TGA results shows the presence of an endothermic peak corresponding to the weight loss of about 18% in the temperature range, 25–250 °C (FeCuNi-LDH turns into FeCuNi-280). This peak can be attributed to the desorption of the surface water and may be due to the removal of strongly bonded coordinate water molecules from the framework of FeCuNi-LDH and oxidation of complexes. Further increase in temperature leads to the weight loss of ~5% in the temperature range 250–550 °C, caused the reduction of Fe_2O_3 to Fe_3O_4 (Sarkari et al., 2012). There is no significant weight loss after 550 °C (< 1%) which indicates that no structural changes occur in FeCuNi-550 (FeCuNi-280 turns into FeCuNi-550). The increase in temperature from 25° to 700 °C leads to the weight loss of about 24%. Based on the obtained data from the TG analysis, the synthesis of FeCuNi-LDH, FeCuNi-280 and FeCuNi-550 was done. The additional information regarding TGA curve of the FeCuNi-LDH are presented in Fig. S1 in the Supplementary material section.

The specific surface area was estimated using the BET method. Surface area measurements of all three sorbents, FeCuNi-LDH, FeCuNi-280 and FeCuNi-550, were recorded to follow the effect of calcination. The BET analysis of the samples has confirmed a large surface area of FeCuNi-280, about 2 times larger compared with FeCuNi-LDH, and about 6 times larger than FeCuNi-550. The BET results also showed that nanosorbent FeCuNi-280 has higher pore volume and lower pore size compared with FeCuNi-LDH and FeCuNi-550. FeCuNi-LDH has a BET surface area of 93.85 m^2/g with a broad BJH (Barrett-Joyner-Halenda) pore size distribution, with a peak at 20 nm, and a certain amount of pores at around 4 nm. The micropore (pores below 2 nm) area, measured by the t-plot method, was 8.1 m^2/g. The FeCuNi-280 nanosorbent has the BET surface area of 166.84 m^2/g. By the BJH pore size method, the sample predominantly contains pores of around 4.9 nm. The FeCuNi-280 nanosorbent is a classical IV-type of isotherm with N_2 hysteresis loops, revealing the presence of mesoporous structures according to the IUPAC classification of porous materials. The FeCuNi-550 nanosorbent has a significantly lower surface area, 25.1 m^2/g, and very low porosity. The large surface area and mesoporous structure of FeCuNi-280 allow the rapid diffusion and this offer more active sites for sorption of organic pollutants on its surface. The sorption capacity of FeCuNi-280 is higher for 1.5 times from FeCuNi-LDH, and 8 times from

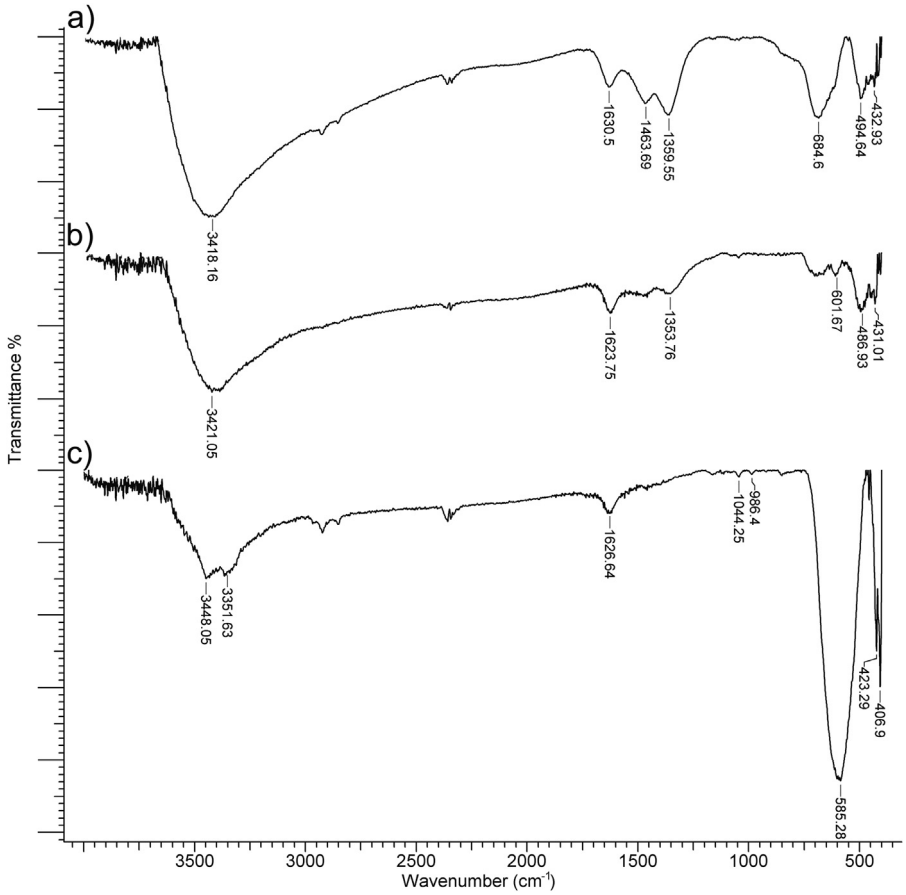

Fig. 1. FTIR spectroscopy results of: a) FeCuNi-LDH, b) FeCuNi-280 c) FeCuNi-550.

FeCuNi-550, after calcination due to the appearance of the microporous texture and large surface area, as will be observed in the dye removal section. The additional information regarding BET results are presented in Table S1 and Fig. S2 in Supplementary material section.

The FTIR spectroscopy results of FeCuNi-LDH (a), FeCuNi-280 (b) and FeCuNi-550 (c) are presented in Fig. 1. In the FTIR spectrum of FeCuNi-LDH the band at 1630 cm^{-1} can be attributed to the deformation vibration of δ_{OH} group of water which corresponds to the presence of crystal water in the structure FeOOH. The FTIR spectrum shows broad intense bands at 3418 and 685 cm^{-1}, which correspond to frequency, shape and intensity of the ν_{OH} and δ_{OH} vibration of the OH group from the bond H-O···Fe, respectively. The FTIR spectrum shows the band at 495 cm^{-1}, which corresponds to frequency, shape and intensity from stretching the Fe–O group. The band on 1464 cm^{-1} and about 1360 cm^{-1}, by shape, intensity and frequency can be attributed to deformation vibration of OH (δ_{OH} in the plane). The frequencies of those vibrations generally indicate a *β2* - modification of FeOOH. Valent Fe–O···Fe vibration may be attributed to the band of medium intensity at about 685 and 433 cm^{-1}. Surface Fe atoms are octahedral coordinated with H_2O ligands, forming the first hydrate layer. In the spectrum of FeCuNi-280 and FeCuNi-550, there is probably a change in the structure of FeOOH, from of α - Fe_2O_3 to γ - Fe_2O_3. FTIR spectra of FeCuNi-280 and FeCuNi-550 exhibited vibrations in the region 400–600 cm^{-1}, which can be attributed to the vibrations of M − O (M = Cu, Ni and Fe), which confirms the formation of CuO, NiO and Fe_2O_3 nanoparticles. In the case of Fe_2O_3, the bands appearing at 1624 and 1627 cm^{-1} can be attributed to the angular deformation of water δH − OH, while the band appearing at 3421 and 3448 cm^{-1} can be assigned to the O − H stretching of water.

To further elucidate the structure of FeCuNi-LDH, FeCuNi-280 and FeCuNi-550, the XRD spectra of the tested sorbents were analyzed. XRD data of the FeCuNi-LDH sample shows amorphous structure, due to the noise it can be identified several major peaks that were located at approximately 35.4° and 38.7° from the copper oxide and β-iron oxide hydrate. After calcination, the layered structure of the FeCuNi-LDH material was destroyed and changed into triple-metal nanosorbents FeCuNi-280 and FeCuNi-550 (non-stoichiometric oxides). The diffractogram for FeCuNi-280 sample indicates the sample consists of both amorphous and crystalline fractions. The predominant crystalline phase is CuO. Also, the peak at 63° 2theta indicates another phase, probably comes from $NiFe_2O_4$-cubic (Xianhua et al., 2017). The sample FeCuNi-550 exhibited several diffraction peaks (about 30.3°, 35.7°, 63.0°) that correspond to spinel $NiFe_2O_4$-cubic and tenorite CuO-monoclinic. The additional information regarding XRD for nanosorbents are presented in Fig. S3 in the Supplementary material section.

SEM analysis (Fig. 2) confirmed the presence of agglomerated particles with nonuniform size. SEM and EDS data for the nanosorbent FeCuNi-550 was not collected because the material is magnetic, and the device could not make micrographs for such (magnetic) materials. The FeCuNi-LDH consisted of nearly spherical particles with the size distribution of approximately 25 nm, which appears to show that the shards are aggregates of smaller particles. After the calcination at 280 °C, the morphological features changed compared with FeCuNi-LDH and showed that the agglomerate size was reduced compared to the FeCuNi-LDH. The FeCuNi-280 consisted of aggregates below 50 μm showing that they are aggregates formed by small nanograins. The sample was highly textured. The large range in the size of the distribution can be attributed to the growth and agglomeration of smaller particles, perhaps due to calcination.

The local elemental composition of FeCuNi was investigated by EDS analysis and confirms the presence of O, Fe, Cu and Ni in the structure of FeCuNi-LDH and FeCuNi-280 (Fig. 2. c, d). EDS analysis was carried

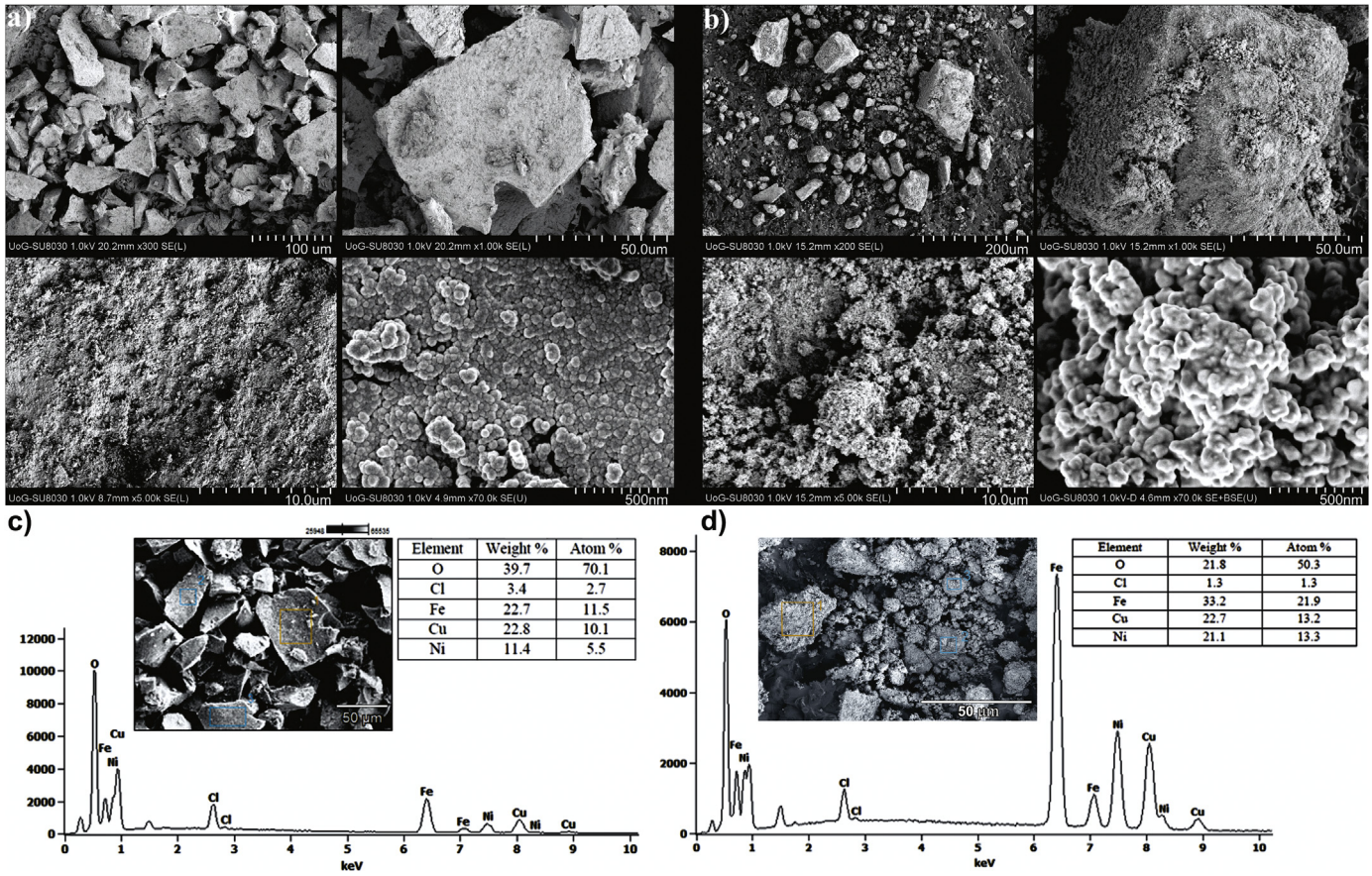

Fig. 2. SEM micrographs for: a) FeCuNi-LDH, b) FeCuNi-280 and EDS spectra for: c) FeCuNi-LDH, d) FeCuNi-280.

out at different points of each sample and the composition didn't show large variations on the surface, suggesting that the applied process for the synthesis of the nanosorbent is effective with homogenity in composition. As can be seen from the EDS spectra of FeCuNi-280, the atomic ratio of Fe, Cu and Ni in the mesoporous ternary oxide is in good agreement with the ratio of $FeCl_3$, $FeCl_2$, $CuCl_2$ and $NiCl_2$ reactants. The decrease in the weight % and atom % of oxygen is the consequence of the removed water at FeCuNi-280.

3.2. Sorption and removal of RB19 dye via FeCuNi-280

3.2.1. Effect of contact time

The effect of contact time on the sorption of various nanosorbents FeCuNi-LDH, FeCuNi-280 and FeCuNi-550 was studied between 0 and 180 min in order to define the influence of contact time on the sorption capacity of the sorbents (Fig. 3a). The results indicate that the sorption increases with an increase in contact time, where the sorption occurred in two steps. The initial step was fast and lasted for 20 min for FeCuNi-LDH and the nanosorbent FeCuNi-280 (sorption capacity rapidly increasing). In the second step, the sorption capacity gradually increased, reaching an equilibrium value in approximately 120 min. The sorption on FeCuNi-550 was rapid and equilibrium was reached after 5 min. However, the experimental data were measured till 240 min to make sure that full equilibrium was attained. The sorption efficiency of RB19 was higher in the beginning due to the fact that all sorbent sites were vacant in the beginning and their sorption capabilities were high for RB19. After that, the sorption speed decreased to a constant value with an increase in contact time because all available sites were covered and there was no active site available for binding. The maximum sorption capacity of RB19 on FeCuNi-280 was 325.75 mg/g (the RB19 concentration of 200 mg/dm^3), while the maximum sorption capacity for FeCuNi-LDH and FeCuNi-550 was approximately 1.4 (238.71 mg/g) and 8.2 (39.94 mg/g) times smaller, respectively. Therefore, due to the considerably higher sorption capacity of nano FeCuNi-280 in comparison with FeCuNi-LDH and FeCuNi-550, for all subsequent experiments nano FeCuNi-280 was exclusively used.

3.2.2. The point of zero charge and effects of initial pH on sorption

The pH at the point of zero charge (pH_{PZC}) of the nanosorbent FeCuNi-280 was determined by the solid addition method of simplified mass potentiometric titration (Balderas-Hernández et al., 2006; Cardenas-Peña et al., 2012). pH_{PZC} indicates the linear range of pH sensitivity and the sorption ability of the surface. The value of pH_{PZC} for nanosorbent FeCuNi-280 is found to be 8.66. Generally, when the pH of the solution is lower than 8.66, the surface of the FeCuNi-280 gets positively charged and the FeCuNi-280 behaves as a Brönsted acid and as an anion exchanger. The surface of the FeCuNi-280 is negatively charged when the pH of the solution is higher than 8.66 and the FeCuNi-280 behaves as a Brönsted base and as a cation exchanger (Cardenas-Peña et al., 2012). When the pH of the solution is higher than 8.66, the Brönsted basic site such as OH^- groups, the moderately basic sites as Ni–O, Fe–O and Cu–O and the strongly basic sites assigned to the strong Lewis basic sites as unsaturated O^{2-} ions, can be sorbent of cations. There are Lewis acid sites at cooperative ferrous, nickel and copper ions (Fe^{II}, Ni^{II} and Cu^{II}) centers for sorption of anions, when the pH of the solution is lower than 8.66.

As shown in Fig. 3b), when pH was raised from 2 to 10 the sorption capacity of RB19 decreased from 325.75 to 164.78 mg/g for contact time 240 min. However, the sorption capacity for RB19 slightly decreased for about 40 mg/g, when pH was raised from 2 to 6. That is in accordance with the obtained value of pH_{PZC}. The sulfonic groups in RB19 molecule are dissociated, and negatively charged ($–SO_3^-$).

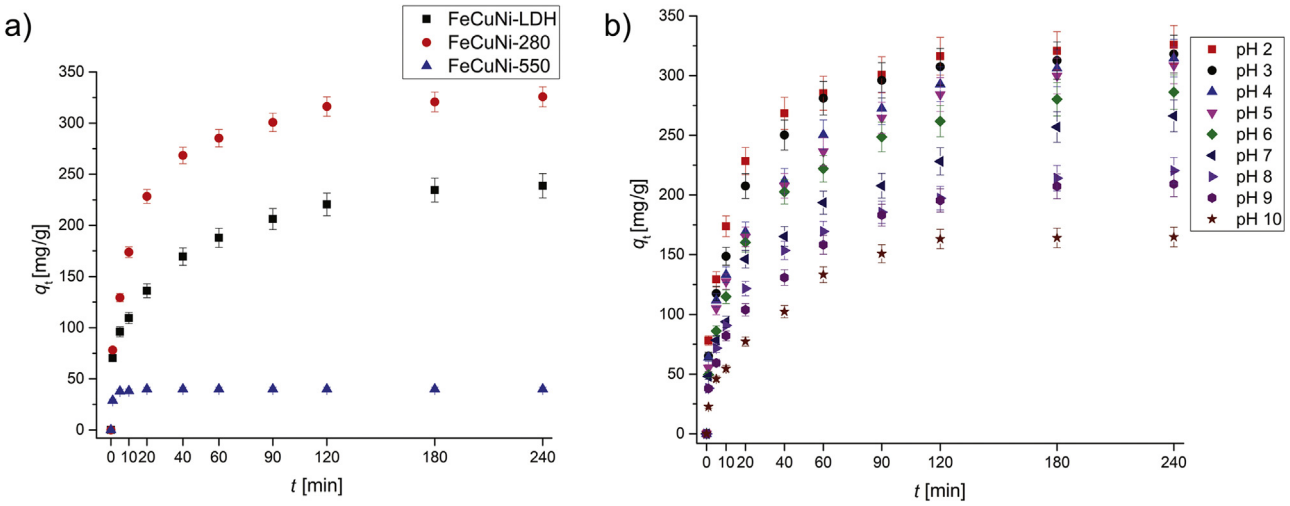

Fig. 3. a) Results of effects of contact time on the sorption of RB19 on FeCuNi-LDH, FeCuNi-280 and FeCuNi-550, b) Results of effect of pH on the sorption of RB19 on FeCuNi-280 (c_0: 200 mg/dm^3; sorbent dose: 0.6 g/dm^3, steering speed: 280 rpm, temperature: 20 °C).

Because of that dye molecules are bound by electrostatic attractions with protonate groups in FeCuNi-280. Conversely, at higher pH more –OH$^-$ were present in solution and compete with the sulfonic groups, which led to a decrease in the number of active sites for dye adsorption. The removal of anionic dye by sorption increases at low pH and decreases at high pH. On the basis of the above results, the optimum pH value is found to be from 2.0 to 6.0. The maximum sorption occurs in that range because of the electrostatic attraction. This is very important characteristic when this material is applied for the treatment of wastewater whose pH is approximately neutral. Also, it can be seen from these results that this nanosorbent can be applied in the distinctly alkaline environment, but with somewhat less sorption efficiency. However, further sorption studies were carried out at pH 2 (where sorption capacity is the largest).

3.2.3. *Effect of sorbent dose, stirring speed and initial concentration*

The effect of nanosorbent FeCuNi-280 dose on RB19 uptake was investigated. From Fig. 4a) it can be seen that the sorption capacity of RB19 decreases with an increase in the sorbent dose. This may be attributed to overlapping or aggregation of sorption sites (Anbia and Salehi, 2012). However, the removal efficiency (*RE* %) of RB19 was increased from 21% to 100%, when the FeCuNi-280 dose was increased from 0.125 to 0.6 g/dm^3. Increase in sorption with the FeCuNi-280 dose could be attributed to increased surface area and the availability of more sorption sites (Iriel et al., 2018). Further increase of the sorbent dose did not affect the removal efficiency (*RE* %) of RB19. This sorbent dose (0.6 g/dm^3) was used for further experiments.

The results showed on Fig. 4b) that an increase in stirring speed from 150 to 280 rpm significantly increases removal efficiency (*RE* %) from 84% to 98%. With the increase of stirring speed, the boundary layer thickness decreases (which results in a reduction in surface film resistance) and probability of collision between the dye and sorbent particles increases. The stirring speed of 280 rpm was used in all experiments.

The experimental data from Fig. 4c) reveal that the sorption capacity enhanced by increasing the initial dye concentration (enhancing the driving forces) (Abbas et al., 2014; Hu and Wang, 2016). With the increase of the initial RB19 concentration from 50 to 700 mg/dm^3, the sorption capacity increases from 82.8 to 480.8 mg/g, i.e., about 5.8 times. The increase in sorption capacity with the increase of initial dye concentration, can be explained by the growing effect of driving force (the concentration gradient).

3.2.4. *Kinetics study*

The estimated kinetics constants for the sorption process after applying the equation from 4 to 7 for different initial RB19 concentrations are presented in Table 1. The determination coefficient values for sorption RB19 on nanosorbent FeCuNi-280 were determined to be in the range from 0.942 to 0.993 for pseudo-first order. r^2 values decrease with increase of initial concentration and show that results do not fit the pseudo-first-order well. The values of the relative deviation range from 3.61% to 8.01% with the increase of initial concentration.

The non-linear fit of kinetics data reveal that the pseudo second order model shows the greater value of determination coefficient (r^2) and that calculated $q_{e,cal}$ values are approximate to experimental $q_{e,exp}$ values. The value of relative deviation is in the range from 0.07% to 2.35%. Thus, it can be concluded that the pseudo-second-order model better describe kinetics sorption for RB19 onto triple-metal nanosorbent FeCuNi-280. This suggests that the rate-controlling step in the sorption process is the chemical interaction between functional groups of FeCuNi-280 and RB19 in the solution.

The values of determination coefficient for Chrastil's diffusion model were higher than for all used models (0.998-1), also the values of relative deviation are maximum 1.3%. The values of diffusion resistance coefficient (n) were in the range from 0.271 to 0.426, which indicates that the sorption process was strongly limited by diffusion resistance.

To investigate the rate determining step of the sorption process, the Weber-Morris intra-particle diffusion model was utilized. The values of the determination coefficient ranged between 0.92 and 1. The kinetics data showed that the plot q_t versus $t^{0.5}$ had three linear segments (for concentrations higher than 100 mg/dm^3). The kinetics data showed that the plot q_t versus $t^{0.5}$ had two linear segments at concentrations lower than 100 mg/dm^3 due to faster sorption (equilibrium is reached in about 10 min). The plots (q_t versus $t^{0.5}$) do not pass the origin, that indicated the rate determining step of sorption was not only controlled by an intra-particle diffusion mechanism but also controlled by some other mechanisms. The rate of sorption was faster at the beginning of the experiment, as expected, because of the values of K_{id1} obtained from the intra-particle diffusion model were higher for the first stage than for the second stage (K_{id2}). Values of K_{id1} and K_{id2} increased with the increase of initial concentration RB19 because of higher driving forces. Values of C_1 and C_2 were proportional to the thickness of boundary layer and increased with an increase of the initial concentration of RB19. The values of C_2 were higher than those of C_1. Values of K_{id2} and C_2 suggested that the intra-particle diffusion was slower and that was

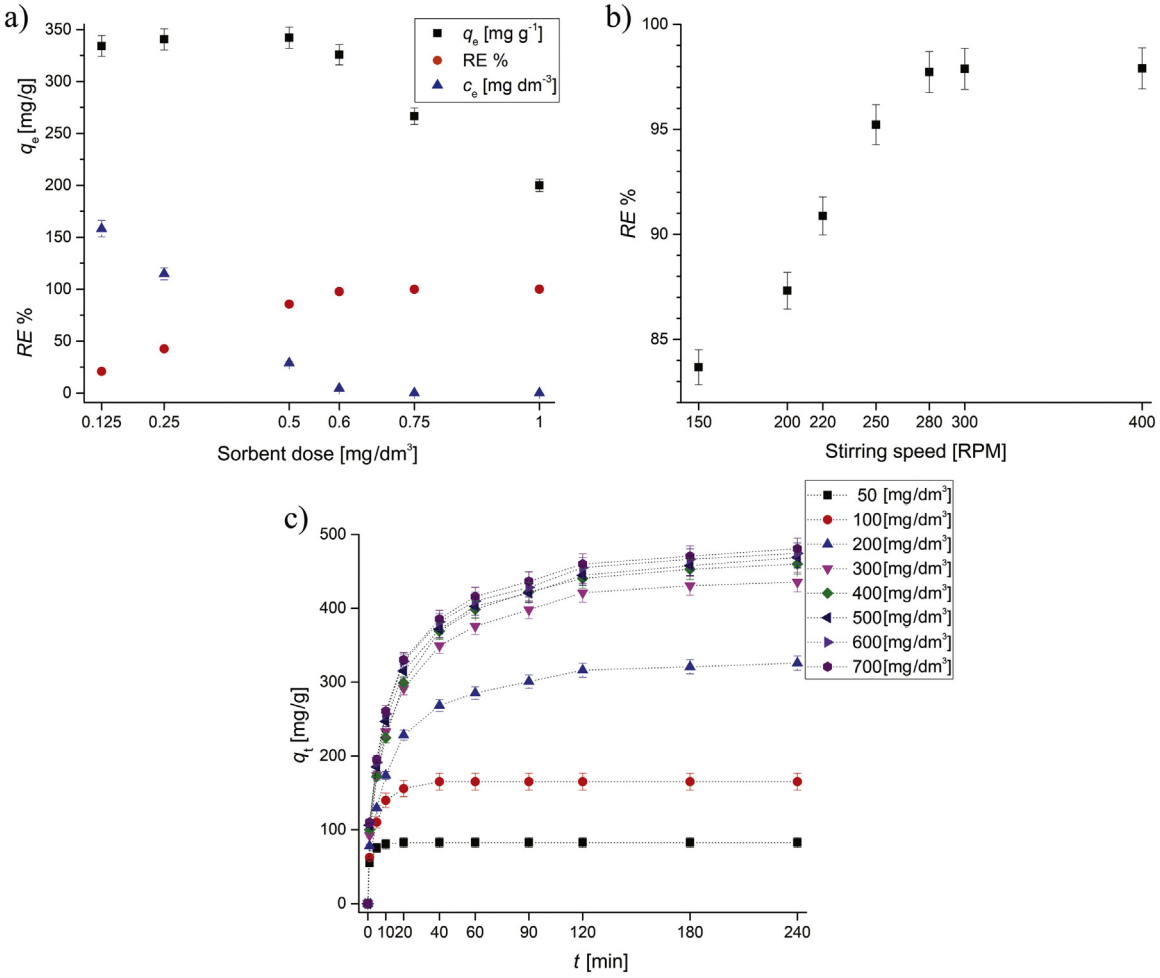

Fig. 4. Results of: a) Effect of sorbent dose, b) effect of stirring speed and c) effect of initial concentration on RB19 removal using nanosorbent FeCuNi-280.

the rate-controlling step in the sorption process. The investigated sorption process did not only conform to the model particle diffusion, but also included two significant limiting factors: surface reaction and diffusion. The additional information regarding the plots of q_t vs. t for pseudo-first, pseudo-second order, Chrastil's diffusion model and plot of q_t vs. $t^{1/2}$ for the intra-particle diffusion model for different initial RB19 concentrations are presented in Fig. S4 in Supplementary material section.

Table 1
Parameters of kinetics modelling for sorption of RB19 onto nanosorbent FeCuNi-280.

Parameters	50 [mg/dm^3]	100 [mg/dm^3]	200 [mg/dm^3]	300 [mg/dm^3]	400 [mg/dm^3]	500 [mg/dm^3]	600 [mg/dm^3]	700 [mg/dm^3]
$q_{e,exp}$ [mg/g]	82.83	165.17	325.75	435.58	460.03	468.78	474.29	480.79
Pseudo-first order								
$q_{e,cal}$ [mg/g]	79.84	158.74	303.86	403.60	429.07	432.46	436.82	442.25
k_1 [1/min]	1.159	0.283	0.086	0.083	0.072	0.083	0.089	0.089
r^2	0.993	0.958	0.948	0.947	0.950	0.942	0.945	0.944
Pseudo-second order								
$q_{e,cal}$ [mg/g]	84.78	170.80	329.89	439.95	470.05	470.98	474.62	480.26
k_2 [g/mg min]	0.021	0.003	3.79 10^{-4}	2.68 10^{-4}	2.17 10^{-4}	2.52 10^{-4}	2.68 10^{-4}	2.67 10^{-4}
r^2	1	0.991	0.981	0.984	0.982	0.981	0.982	0.982
Chrastil model								
$q_{e,cal}$ [mg/g]	82.82	165.79	322.88	433.17	457.96	463.11	468.74	474.72
n	0.271	0.426	0.388	0.387	0.409	0.370	0.373	0.371
k_c [dm^3/g min]	0.415	0.172	0.039	0.035	0.035	0.033	0.035	0.035
r^2	1	1	0.998	0.999	0.999	0.998	0.998	0.998
Intraparticle diffusion model								
K_{id1} [mg/g min$^{1/2}$]	6.360	34.755	41.888	54.787	57.198	58.001	59.907	60.355
C_1	27.375	18.167	26.302	32.968	30.256	37.950	39.322	40.703
r^2	0.920	0.936	0.953	0.951	0.970	0.948	0.944	0.942
K_{id2} [mg/g min$^{1/2}$]	0.001	0.533	10.150	15.134	15.161	15.175	15.216	15.543
C_2	82.833	158.66	205.08	255.42	276.76	279.77	287.39	290.32
r^2	1	0.932	0.996	0.993	0.979	0.971	0.980	0.981

Table 2
Parameters for Langmuir, Freundlich, Sips and Brouers - Sotolongo isotherm models of RB19 sorption on triple-metal nanosorbent FeCuNi-280.

Isotherm	Calculated parameters								Relative deviation [%]
	$q_{e,exp}$	480.79							
Langmuir	q_m	470.01	K_L	0.568			r^2	0.994	2.24
Freundlich	K_F	204.97	n	6.469				0.850	
Sips	q_m	479.17	b_S	0.518	n_S	0.829		0.999	0.34
B–S	q_m	465.91	K_W	0.458	α	0.613		0.992	3.09

3.2.5. Sorption isotherms

The equilibrium data were fitted with Langmuir, Freundlich, Sips and Brouers - Sotolongo models, and model parameters were shown in Table 2. The additional information regarding the non-linear fit of isotherms models (the plot of q_e vs. c_e) was shown in Fig. S5 in Supplementary material section. The determination coefficient (r^2) and relative deviation of q_m from $q_{e,exp}$ were used for the accurate estimation of applied models. Based on r^2 and relative deviation in Table 2, it can be concluded that among the applied models, only the following are appropriate: Langmuir, Sips and Brouers–Sotolongo isotherm models. The Sips isotherm model was one of the best fitted models in this study. The maximum sorption capacity of nanosorbent FeCuNi-280 suggested by Sips, Langmuir and Brouers - Sotolongo isotherm models were very similar to the experimental $q_{e,exp}$, while for FeCuNi-280 sorption capacity, q_m, calculated from Freundlich isotherm model was not consistent with the experimental $q_{e,exp}$ value.

From the experimental data for all of initial RB19 concentrations, the values of R_L for nanosorbent FeCuNi-280 decreased from 0.034 to 0.002 as the initial concentration increased from 50 to 700 mg/dm^3. That showed the reaction became more favorable at higher initial RB19 concentrations under the condition used in this study.

Based on the Langmuir, Sips and Brouers - Sotolongo isotherm models, it can be concluded that the sorption is not only monolayer to homogeneous sorption sites but can have heterogeneous character.

3.2.6. Energy of activation and thermodynamics

The activation energy increased from 9.42 to 20.56 kJ/mol with the increase of initial RB19 concentration from 50 to 700 mg/dm^3. The values of activation energy suggest that physical sorption processes were an important process in the sorption of RB19 onto nanosorbent FeCuNi-280 (Kuo et al., 2008).

The enthalpy change was found to be from 6.98 to 18.13 kJ/mol, and the positive value of ΔH° indicated the endothermic nature of sorption.

3.3. Comparative analysis of sorption capacity of various sorbents

For the purpose of comparison, Table 3 presents the maximum sorption capacity of nanosorbent FeCuNi-280 for RB19 and other parameters in this study, with some data for different sorbents reported in the literature.

It is clear from Table 3 that the nanosorbent FeCuNi-280 showed better sorption capacity than all of the previously used sorbents for the removal of RB19 dyes, except Chitosan film. It is obvious that the sorption capacities of nanosorbent FeCuNi-280 for anionic dyes RB19 were acceptable, compatible, and comparable with the results of other alternative and low-cost sorbents reported in the literature earlier.

3.4. Desorption of RB19 and reusing of triple-metal nanosorbent

Regeneration and reusability of sorbents is an important factor for industrial and practical applications because of reduction of the need for new amount of sorbent and lowering of synthesis costs of the sorbent materials. It was found that for FeCuNi-280, the removal efficiency (*RE* %) decreased from 98.84% to 92.40% in the first three cycles and then reached 86.47% in the fourth cycle and the fifth cycle reached 83.32%. The maximum desorption efficiency by NaOH was obtained after 10 min and amounted about 72% in the first desorption cycle. In the next cycles desorption efficiency by using NaOH was higher than 92%. The minor decrease of the sorption capacity can be attributed to the loss of the sorbents in the sorption-desorption processes and the irreversible binding (chemisorption) of RB19 on FeCuNi-280. Contrary to NaOH, desorption of RB19 using NaCl solution was very low with *DE* % of 22.58%. Therefore, the FeCuNi-280 can be reutilized, with previously desorption using NaOH. Nearly all the sorption sites could be recovered from the FeCuNi-280.

3.5. Removal of RB19 from wastewater

In order to confirm the efficiency of triple-metal nanosorbent FeCuNi-280 for the removal of RB19 in wastewater, it was made synthetic wastewater based on the real wastewater from dyeing process. The exact composition of the dye bath and wastewater are given by the textile company; usually 20% of the dyes and 100% of all applied assisting chemicals remain in the exhausted dyeing bath. The additional information regarding of chemical composition and characteristics of synthetic wastewater in the dyeing process is presented as Supplementary material in Table S2 in the Supplementary material

Table 3
Comparison of maximum sorption capacity for RB19 and other parameters of triple-metal nanosorbent FeCuNi-280 with some reported data in the literature.

Sorbents	pH	Sorbent dose [g/dm^3]	Sorption capacities [mg/g]	Maximum RB19 concentration [mg/dm^3]	References
Chitosan film	6.8	0.007	822.40	800	(Nga et al., 2016)
Nanosorbent FeCuNi-280	**2.0**	**0.600**	**480.80**	**700**	**This study**
CS hollow fibers	3.5	0.200	454.50	70	(Mirmohseni et al., 2012)
Hexagonal MgO	7.8	0.100	250.00	100	(Nga et al., 2013)
Functionalized MWCNT	3.0	0.300	211.02	250	(Karimifard and Moghaddam, 2016)
Modified bentonite	1.5	0.030	206.60	282	(Özcan et al., 2007)
MgO nanoparticles	8.0	0.200	166.70	300	(Moussavi and Mahmoudi, 2009)
Mycelium pellets of Penicillium oxalicum	7.0	0.025	159.00	not available	(Zhang et al., 2003)
Wheat bran	1.5	0.500	117.60	150	(Çiçek et al., 2007)
L-Arginine-functionalized Fe_3O_4	3.0	0.740	125.00	200	(Dalvand et al., 2016)
Fe_3O_4 nanoparticles modified by pyrrole	3.0	0.020	112.40	50	(Shanehsaz et al., 2015)
Magnetite nanoparticles loaded tea waste	3.0	0.500	87.72	not available	(Madrakian et al., 2012)
SiO_2-NH_2-BH	4.0	0.060	72.99	100	(Banaei et al., 2017a)
Modified silica gel	5.0	0.060	37.45	40	(Banaei et al., 2017b)
γ-Fe_2O_3/crosslinked chitosan	6.6	1.00	29.49	30	(Zhu et al., 2010)
Scallop shell	6.0	10.0	12.36	500	(Shirzad-Siboni et al., 2014)

section. The pH of the synthetic wastewater was adjusted by 1 mol/dm^3 HNO_3 solution at 5. The native pH of the synthetic wastewater was used and amounted 9.3. The removal efficiency (*RE* %) decreased for the synthetic wastewater to 76.4% in comparison with the RB19 in deionized water, where the removal efficiency (*RE* %) was 92.6% at pH 5. However, at pH 9.3 the removal efficiency (*RE* %) decreased for the synthetic wastewater to 41.8%. The removal efficiency (*RE* %) at pH 9 for solutions of the RB19 in deionized water was about 62.7%. Decrease in the removal efficiency (*RE* %) with the increase of pH from 5 to 9.3 for synthetic wastewater was in accordance with the obtained results of the effect of pH. The decrease in the removal efficiency (*RE* %) in wastewater was a consequence of the presence of other components, in addition to dye, in the dyeing bath.

4. Conclusions

The synthesis of triple-metal nanosorbents from LDH, their characterization, and removal of RB19 from water and wastewater are investigated. BET analysis of the nanosorbents show that the triple-metal nanosorbent FeCuNi-280 has the highest specific surface area, with dominant mesoporousity, in comparison with the FeCuNi-LDH and FeCuNi-550. The FTIR, XRD, SEM and EDX analysis show differences in the structure of the sorbents as a result of different calcination temperature in synthesis. The maximum sorption capacity of the triple-metal nanosorbent FeCuNi-280 for RB19 regarding to FeCuNi-LDH and FeCuNi-550 is approximately 1.4 and 8.2 times higher, respectively. The maximum removal of RB19 dye by triple-metal nanosorbent FeCuNi-280 is obtained at pH 2, with the sorbent dose of 0.6 g/dm^3 and at the stirring speed of 280 rpm. The kinetics data shows that the sorption of RB19 on triple-metal nanosorbent FeCuNi-280 follows pseudo-second order and the Chrastil model. Based on the determination coefficient and the relative deviation, the Sips model the best fits experimental data, giving calculated maximum sorption capacity of 479.17 mg/g. The values of activation energy indicate physical sorption and the endothermic nature of the sorption of RB19 onto FeCuNi-280. Presented triple-metal nanosorbent FeCuNi-280 can be used for the treatment of wastewater from textile industry in wide range of pH. Finally, FeCuNi-280can be recommended as a promised, efficient and reusable sorbent for the removal of dyes from water and wastewater.

Acknowledgements

The authors would like to thank the Ministry of Education, Science and Technological Development of the Republic of Serbia for supporting this work (Grant no TR 34008).

Appendix A. Supplementary material

Supplementary data associated with this article can be found in the online version at http://dx.doi.org/10.1016/j.ecoenv.2018.05.015.

References

Abbas, M., Kaddour, S., Trari, M., 2014. Kinetic and equilibrium studies of cobalt adsorption on apricot stone activated carbon. J. Ind. Eng. Chem. 20, 745–751. http://dx.doi.org/10.1016/j.jiec.2013.06.030.

Anbia, M., Salehi, S., 2012. Removal of acid dyes from aqueous media by adsorption onto amino-functionalized nanoporous silica SBA-3. Dyes Pigments 94, 1–9. http://dx.doi.org/10.1016/j.dyepig.2011.10.016.

Auta, M., Hameed, B.H., 2014. Optimized and functionalized paper sludge activated with potassium fluoride for single and binary adsorption of reactive dyes. J. Ind. Eng. Chem. 20, 830–840. http://dx.doi.org/10.1016/j.jiec.2013.06.013.

Balderas-Hernández, P., Ibanez, J.G., Godinez-Ramirez, J.J., Almada-Calvo, F., 2006. Microscale environmental chemistry: Part 7. estimation of the point of zero charge (pzc) for simple metal oxides by a simplified potentiometric mass titration method. Chem. Educ. 11, 267–270. http://dx.doi.org/10.1333/s00897061012a.

Banaei, A., Ebrahimi, S., Vojoudi, H., Karimi, S., Badiei, A., Pourbasheer, E., 2017a. Adsorption equilibrium and thermodynamics of anionic reactive dyes from aqueous solutions by 2,2-(pentane-1,5-diylbis(oxy)) dibenzaldehyde. Chem. Eng. Res. Des. 123, 50–62. http://dx.doi.org/10.1016/j.cherd.2017.04.032.

Banaei, A., Samadi, S., Karimi, S., Vojoudi, H., Pourbasheer, E., Badiei, A., 2017b. Synthesis of silica gel modified with 2,2′-(hexane-1,6-diylbis(oxy)) dibenzaldehyde as a new adsorbent for the removal of Reactive Yellow 84 and Reactive Blue 19 dyes from aqueous solutions: equilibrium and thermodynamic studies. Powder Technol. 319, 60–70. http://dx.doi.org/10.1016/j.powtec.2017.06.044.

Bergamini, R.B.M., Azevedo, E.B., Raddi de Araújo, L.R., 2009. Heterogeneous photocatalytic degradation of reactive dyes in aqueous TiO_2 suspensions: decolorization kinetics. Chem. Eng. J. 149, 215–220. http://dx.doi.org/10.1016/j.cej.2008.10.019.

Brouers, F., Sotolongo, O., Marquez, F., Pirard, J.P., 2005. Microporous and heterogeneous surface adsorption isotherms arising from Levy distributions. Physica A 349, 271–282. http://dx.doi.org/10.1016/j.physa.2004.10.032.

Cai, J., Zhao, X., Zhang, Y., Zhang, Q., Pan, B., 2018. Enhanced fluoride removal by La-doped Li/Al layered double hydroxides. J. Colloid Interface Sci. 509, 353–359. http://dx.doi.org/10.1016/j.jcis.2017.09.038.

Cardenas-Peña, A.M., Ibanez, J.G., Vasquez-Medrano, R., 2012. Determination of the point of zero charge for electrocoagulation precipitates from an iron anode. Int. J. Electrochem. Sci. 7, 6142–6153.

Chrastil, J., 1990. Adsorption of direct dyes on cotton: kinetics of dyeing from finite baths based on new information. Text. Res. J. 60, 413–416. http://dx.doi.org/10.1177/004051759006000706.

Çiçek, F., Özer, D., Özer, A., Özer, A., 2007. Low cost removal of reactive dyes using wheat bran. J. Hazard. Mater. 146, 408–416. http://dx.doi.org/10.1016/j.jhazmat.2006.12.037.

Dalvand, A., Nabizadeh, R., Ganjali, M.R., Khoobi, M., Nazmara, S., Mahvi, A.H., 2016. Modeling of Reactive Blue 19 azo dye removal from colored textile wastewater using L-arginine-functionalized Fe_3O_4 nanoparticles: optimization, reusability, kinetic and equilibrium studies. J. Magn. Magn. Mater. 404, 179–189. http://dx.doi.org/10.1016/j.jmmm.2015.12.040.

Fathy, N.A., El-Shafey, S.E., El-Shafey, O.I., Mohamed, W.S., 2013. Oxidative degradation of RB19 dye by a novel γ-MnO_2/MWCNT nanocomposite catalyst with H_2O_2. J. Environ. Chem. Eng. 1, 858–864. http://dx.doi.org/10.1016/j.jece.2013.07.028.

Freundlich, H., 1906. Über die adsorption in Lösungen. Z. Phys. Chem. 57, 385–470.

Gök, Ö., Özcan, A.S., Özcan, A., 2010. Adsorption behavior of a textile dye of Reactive Blue 19 from aqueous solutions onto modified bentonite. Appl. Surf. Sci. 256, 5439–5443. http://dx.doi.org/10.1016/j.apsusc.2009.12.134.

Ho, Y.S., McKay, G., 1998. Sorption of dye from aqueous solution by peat. Chem. Eng. J. 70, 115–124. http://dx.doi.org/10.1016/S1385-8947(98)00076-X.

Hu, D., Wang, L., 2016. Adsorption of amoxicillin onto quaternized cellulose from flax noil: kinetic, equilibrium and thermodynamic study. J. Taiwan Inst. Chem. Eng. 64, 227–234. http://dx.doi.org/10.1016/j.jtice.2016.04.028.

Iriel, A., Bruneel, S.P., Schenone, N., Fernández, A.F., 2018. The removal of fluoride from aqueous solution by a lateritic soil adsorption: kinetic and equilibrium studies. Ecotoxicol. Environ. Saf. 149, 166–172. http://dx.doi.org/10.1016/j.ecoenv.2017.11.016.

Karimifard, S., Moghaddam, M.R.A., 2016. Enhancing the adsorption performance of carbon nanotubes with a multistep functionalization method: optimization of Reactive Blue 19 removal through response surface methodology. Process Saf. Environ. Prot. 99, 20–29. http://dx.doi.org/10.1016/j.psep.2015.10.007.

Kumar, A.S.K., Kalidhasan, S., Rajesh, V., Rajesh, N., 2012. Application of cellulose-clay composite biosorbent toward the effective adsorption and removal of chromium from industrial wastewater. Ind. Eng. Chem. Res. 51, 58–69. http://dx.doi.org/10.1021/ie201349h.

Kuo, C.Y., Wu, C.H., Wu, J.Y., 2008. Adsorption of direct dyes from aqueous solutions by carbon nanotubes: determination of equilibrium, kinetics and thermodynamics parameters. J. Colloid Interface Sci. 327, 308–315. http://dx.doi.org/10.1016/j.jcis.2008.08.038.

Lagergren, S., 1898. Zur theorie der sogenannten adsorption geloster stoffe, Kungliga Svenska Vetenskapsakademiens. Handlingar 24, 1–39.

Langmuir, I., 1918. The adsorption of gases on plane surfaces of glass, mica and platinum. J. Am. Chem. Soc. 40, 1361–1403.

Lei, C., Pi, M., Kuang, P., Guo, Y., Zhang, F., 2017. Organic dye removal from aqueous solutions by hierarchical calcined Ni-Fe layered double hydroxide: isotherm, kinetic and mechanism studies. J. Colloid Interface Sci. 496, 158–166. http://dx.doi.org/10.1016/j.jcis.2017.02.025.

Lv, L., He, J., Wei, M., Duan, X., 2006. Kinetic studies on fluoride removal by calcined layered double hydroxides. Ind. Eng. Chem. Res. 45 (25), 8623–8628. http://dx.doi.org/10.1021/ie050363d.

Madrakian, T., Afkhami, A., Ahmadi, M., 2012. Adsorption and kinetic studies of seven different organic dyes onto magnetite nanoparticles loaded tea waste and removal of them from wastewater samples. Spectrochim. Acta A 99, 102–109. http://dx.doi.org/10.1016/j.saa.2012.09.025.

Mahmoud, D.K., Salleh, M.A.M., Karim, W.A.W.A., Idris, A., Abidin, Z.Z., 2012. Batch adsorption of basic dye using acid treated kenaf fibre char: equilibrium, kinetic and thermodynamic studies. Chem. Eng. J. 181–182, 449–457. http://dx.doi.org/10.1016/j.cej.2011.11.116.

McKay, G., Mesdaghinia, A., Nasseri, S., Hadi, M., Aminabad, M.S., 2014. Optimum isotherms of dyes sorption by activated carbon: fractional theoretical capacity & error analysis. Chem. Eng. J. 251, 236–247. http://dx.doi.org/10.1016/j.cej.2014.04.054.

Mirmohseni, A., Dorraji, M.S.S., Figoli, A., Tasselli, F., 2012. Chitosan hollow fibers as effective biosorbent toward dye: preparation and modeling. Bioresour. Technol. 121, 212–220. http://dx.doi.org/10.1016/j.biortech.2012.06.067.

Moghaddam, S.S., Moghaddam, M.R.A., Arami, M., 2010. Coagulation/flocculation process for dye removal using sludge from water treatment plant: optimization through response surface methodology. J. Hazard. Mater. 175, 651–657. http://dx.doi.org/10.1016/j.jhazmat.2009.10.058.

Moussavi, G., Mahmoudi, M., 2009. Removal of azo and anthraquinone reactive dyes from industrial wastewaters using MgO nanoparticles. J. Hazard. Mater. 168, 806–812. http://dx.doi.org/10.1016/j.jhazmat.2009.02.097.

Nga, N.K., Chinh, H.D., Hong, P.T.T., Huy, T.Q., 2016. Facile preparation of chitosan films for high performance removal of reactive blue 19 dye from aqueous solution. J. Polym. Environ. 25, 146–155. http://dx.doi.org/10.1007/s10924-016-0792-5.

Nga, N.K., Hong, P.T.T., Lam, T.D., Huy, T.Q., 2013. A facile synthesis of nanostructured magnesium oxide particles for enhanced adsorption performance in reactive blue 19 removal. J. Colloid Interface Sci. 398, 210–216. http://dx.doi.org/10.1016/j.jcis.2013.02.018.

Özcan, A., Ömeroğlu, Ç., Erdoğan, Y., Özcan, A.S., 2007. Modification of bentonite with a cationic surfactant: an adsorption study of textile dye Reactive Blue 19. J. Hazard. Mater. 140, 173–179. http://dx.doi.org/10.1016/j.jhazmat.2006.06.138.

Salleh, M.A.M., Mahmoud, D.K., Karim, W.A.W.A., Idris, A., 2011. Cationic and anionic dye adsorption by agricultural solid wastes: a comprehensive review. Desalination 280, 1–13. http://dx.doi.org/10.1016/j.desal.2011.07.019.

Sarkari, M., Fazlollahi, F., Atashi, H., Mirzaei, A.A., Hosseinpour, V., 2012. Fischer-Tropsch synthesis: development of kinetic expression for a sol-gel Fe-Ni/Al_2O_3 catalyst. Fuel Process. Technol. 97, 130–139. http://dx.doi.org/10.1016/j.fuproc.2012.01.008.

Saeed, A., Iqbal, M., Akhtar, M.W., 2005. Removal and recovery of lead(II) from single and multimetal (Cd, Cu, Ni, Zn) solutions by crop milling waste (black gram husk). J. Hazard. Mater. 117 (1), 65–73. http://dx.doi.org/10.1016/j.jhazmat.2004.09.008.

Shanehsaz, M., Seidi, S., Ghorbani, Y., Shoja, S.M.R., Rouhani, S., 2015. Polypyrrole-coated magnetic nanoparticles as an efficient adsorbent for RB19 synthetic textile dye: removal and kinetic study. Spectrochim. Acta A 149, 481–486. http://dx.doi.org/10.1016/j.saa.2015.04.114.

Shirzad-Siboni, M., Khataee, A., Vafaei, F., Joo, S.W., 2014. Comparative removal of two textile dyes from aqueous solution by adsorption onto marine-source waste shell: kinetic and isotherm studies. Korean J. Chem. Eng. 31, 1451–1459. http://dx.doi.org/10.1007/s11814-014-0085-4.

Wang, H., Li, Q., He, N., Wang, Y., Sun, D., Shao, W., Yang, K., Lu, Y., 2009. Removal of anthraquinone reactive dye from wastewater by batch hydrolytic–aerobic recycling process. Sep. Purif. Technol. 67, 180–186. http://dx.doi.org/10.1016/j.seppur.2009.03.018.

Weber Jr, W.J., Morris, J.C., 1963. Kinetics of adsorption on carbon from solution. J. Sanit. Eng. ASCE 89, 31–59.

Witek-Krowiak, A., 2012. Analysis of temperature-dependent biosorption of Cu2+ ions on sunflower hulls: kinetics, equilibrium and mechanism of the process. Chem. Eng. J. 192, 13–20. http://dx.doi.org/10.1016/j.cej.2012.03.075.

Xianhua, H., Xiaoqin, T., Shejun, H., Xinyu, W., Yumei, G., Xiang, L., 2017. One-pot Synthesis of Nano-$NiFe_2O_4$ Pinning on the Surface of the Graphite Composite as Superior Anodes for Li-ion Batteries. Rare Met. Mater. Eng. 46 (5), 1169–1175. http://dx.doi.org/10.1016/S1875-5372(17)30131-5.

Xiao, J., Zhang, H., Xia, Y., Li, Z., Huang, W., 2016. Rapid and high-capacity adsorption of sulfonated anionic dyes onto basic bismuth (III) nitrate via bidentate bridging and electrostatic attracting interactions. RSC Adv. 6, 39861–39869. http://dx.doi.org/10.1039/C6RA03055F.

Zhang, S.J., Yang, M., Yang, Q.X., Zhang, Y., Xin, B.P., Pan, F., 2003. Biosorption of reactive dyes by the mycelium pellets of a new isolate of Penicillium oxalicum. Biotechnol. Latt. 25, 1479–1482.

Zhu, H.Y., Jiang, R., Xiao, L., Li, W., 2010. A novel magnetically separable γ-Fe_2O_3/crosslinked chitosan adsorbent: preparation, characterization and adsorption application for removal of hazardous azo dye. J. Hazard. Mater. 179, 251–257. http://dx.doi.org/10.1016/j.jhazmat.2010.02.087.

Zubieta, C.E., Messina, P.V., Luengo, C., Dennehy, M., Pieroni, O., Schulz, P.C., 2008. Reactive dyes remotion by porous TiO_2-chitosan materials. J. Hazard. Mater. 152, 765–777. http://dx.doi.org/10.1016/j.jhazmat.2007.07.043.